RESEARCH ARTICLE

ADVANCED FUNCTIONAL MATERIALS
www.afm-journal.de

Deep Learning-Enabled Self-Powered Stretchable Triboelectric Sensor Array for Intelligent Posture Monitoring and Regulation

Juan Tao, Junjie Huang, Jiahui Tong, Jiaqi Xu, Shaoyu Ma, Rongrong Bao, Xiaohan Wu, Shi-Jin Ding,* and Caofeng Pan**

The growing trend toward proactive health management drives the need for intelligent motion monitoring systems integrating stretchability, high sensitivity, and deep learning-driven real-time analytics for adaptive posture management. Herein, a deep learning-enabled self-powered stretchable triboelectric sensor (STS) system is introduced for intelligent posture recognition. $Ti_3C_2T_x$ (MXene) nanosheets are strategically integrated into distinct layers of the STS to enhance its output performance through multifunctional mechanisms, achieving an angular resolution of ≈1° and an angle sensitivity of 0.56 V/°. By integrating the STS with an augmented reality (AR) system, real-time fitness monitoring and instant feedback are provided to facilitate continuous adjustment of users' postures. Furthermore, an STS array integrated with a patterned shielding layer is developed to monitor and warn against fatigue states during complex cervical spine postures. Leveraging a convolutional neural network (CNN) algorithm, intelligent recognition of 14 distinct postures is achieved with 98.7% accuracy. The trained model is deployed on a smartphone to enable intelligent recognition results and reminder functions. This self-powered, deep learning-driven system bridges flexible sensing with real-time health intervention, offering scalable solutions for elderly care, sports rehabilitation, and occupational health monitoring.

1. Introduction

The shift toward proactive health management has heightened demand for human motion monitoring systems that optimize dynamic postures via closed-loop biofeedback for personalized health assessment.[1,2] Various systems exist to capture motion signals from joints (e.g., wrist, knee, ankle), primarily using inertial measurement units,[3] strain sensors,[4,5] and optical fiber sensors.[6] However, these technologies suffer from critical limitations: large form factors (typically over 10 cm^3), high Young's modulus, and complex data processing.[1] Such drawbacks hinder real-time monitoring and adaptive feedback in dynamic health scenarios, necessitating conformal, wearable, and direct-contact sensing systems. Flexible/stretchable epidermal electronics present a promising alternative by virtue of their skin-conformable designs,[7–10] which deliver essential mechanical properties: wearability, biocompatibility, and portability. Illustrating this paradigm, Lorestani et al. developed a self-powered wearable patch integrating soft biosensing with real-time analytics for simultaneous wireless monitoring of glucose, pH, and temperature.[11] Critically, their inherent capability to conform to curved surfaces renders them uniquely suited for high-fidelity motion tracking in complex postural dynamics.

Flexible/stretchable electronics have evolved primarily through sensing mechanisms such as capacitance,[12–14] resistance,[15,16] piezoelectricity,[17] and triboelectricity.[18] Among these, triboelectric sensors (TES) are based on the coupling of contact electrification and electrostatic induction,[19,20] attracting significant interest for unique advantages: material diversity,[21] superior kinetic energy conversion efficiency,[22,23] and self-powered sensing capabilities.[24] Cheng et al. developed a wireless sensing patch for dynamic motion tracking based on laser-induced graphene.[25] However, its angular detection resolution is ≈15°, rendering it inadequate for sophisticated motion monitoring. High-precision joint angle monitoring requires sensors to meet two core needs: excellent stretchability for dynamic joint deformation[26] and high sensitivity to subtle

---

J. Tao, J. Huang, J. Tong, J. Xu, S.-J. Ding
Jiashan Fudan Institute
Jiaxing, Zhejiang Province 314100, China
E-mail: sjding@fudan.edu.cn

J. Tao, S. Ma, X. Wu, S.-J. Ding
School of Microelectronics
Fudan University
Shanghai 200433, China
E-mail: wuxiaohan@fudan.edu.cn

R. Bao, C. Pan
Institute of Atomic Manufacturing
Beihang University
Beijing 100191, China
E-mail: pancaofeng@buaa.edu.cn

R. Bao, C. Pan
International Research Institute for Multidisciplinary Science
Beihang University
Beijing 100191, China

The ORCID identification number(s) for the author(s) of this article can be found under https://doi.org/10.1002/adfm.202514646

DOI: 10.1002/adfm.202514646

angular changes for accuracy.[27] However, existing electrode materials systems struggle to balance both: traditional ones (e.g., metals,[28] carbon materials,[29] conductive fabrics[30]) lack stretchability, while alternatives like liquid metals[31] and hydrogels[32] risk toxic leakage or moisture-induced instability. Thus, developing stable solid-state stretchable electrodes has become a critical prerequisite for meeting stretchability demands. Meanwhile, enhancing TES output performance is also critical for high sensitivity.[21] Cao et al. reviewed recent optimal strategies of TES, focusing on two core aspects: boosting triboelectric surface charge density and enhancing charge transfer, with material functional modification as a key strategy.[33] MXene ($Ti_3C_2T_x$) nanosheets provide an integrated solution to these dual challenges: high conductivity for efficient charge transfer, strong electronegativity for excellent stretchability/stability.[34,35]

As sensor technology shifts from discrete units to arrays, conventional data analysis methods fail to meet real-time processing needs for complex, high-dimensional datasets. Deep learning—a machine learning frontier using multi-layer neural networks,[36] automatically captures hierarchical data representations via feature abstraction, enabling end-to-end analysis and decision systems.[37] These capabilities have spurred its use in e-skin applications: Lee et al. developed a CNN-based triboelectric system for sign language recognition;[38] Kim's team achieved 87.53% accuracy classifying 100 words with a 3D convolutional algorithm.[39] Integrating deep learning with Internet of Things and AR thus enables a closed-loop "sensing-analysis-feedback" system,[40] supporting active health monitoring via real-time posture recognition and intervention advice. This empowers proactive health management for sub-healthy groups through early risk detection and personalized self-care.

In this work, we report a deep learning-empowered stretchable triboelectric sensor (STS) system for self-powered intelligent posture recognition. MXene ($Ti_3C_2T_x$) nanosheets are strategically integrated into both the electrode and dielectric layers to enhance STS performance. This dual-functional design achieves an angular resolution of $\approx 1°$ and superior detection sensitivity of 0.56 V/°, critical for capturing subtle joint movements. To simulate real-world rehabilitation scenarios, an AR-based fitness interface provides real-time joint angle feedback to guide posture regulation. Additionally, a stretchable triboelectric sensor array (STSA) with a patterned shielding layer monitors cervical spine fatigue, decoding 14 postures from 4-channel signals with 98.7% accuracy. Further, the trained CNN model is deployed on a smartphone for real-time AI predictions, triggering feedback reminders for abnormal head postures. This system, combining self-powered sensing, real-time analytics, and AR feedback, enables proactive posture management, with promise in elderly care, sports rehabilitation, and occupational health monitoring.

2. Results and Discussion

2.1. Design and Working Mechanism of the STS System

Herein, a single-electrode-mode STS was designed for monitoring various joints of the human body, as depicted in **Figure** 1a. A single-unit STS was distributively attached to the elbow, knee, and waist to detect bending angles, while a STSA was developed for cervical spine monitoring, owing to its complex postural dynamics. As previously discussed, stretchability and sensitivity are critical for joint angle sensing. The basic structure and corresponding component materials for each layer of the proposed STS are presented in Figure 1b(i). First, in order to obtain a skin affinity performance, Ecoflex silicon—chosen for its ultrasoftness, biocompatibility, and high electronegativity,[30] serves as the substrate, encapsulation layer, and triboelectric material. Notably, PVA/H_3PO_4 has been widely used as an electrolyte film in solid-state supercapacitors for ion transport,[41] and as an ionic medium in iontronic capacitive sensors.[42] Here, it is employed as a dehydration-resistant solid polymer electrode, leveraging its stretchability and ionic conductivity. The pure PVA/H_3PO_4 acting as a transparent stretchable electrode and pure Ecoflex as a triboelectric layer can comprise a transparent STS (Figure S1, Supporting Information).

To enhance STS performance, MXene ($Ti_3C_2T_x$) nanosheets were incorporated into both the electrode and triboelectric layers at optimized loadings. Specifically, MXene nanosheets were mixed with PVA/H_3PO_4 to form a conductive composite electrode (PVA/H_3PO_4/MXene) to enhance the performance (Figure 1b(ii)). Meanwhile, high-electronegativity MXene was doped into Ecoflex to create an Ecoflex/MXene triboelectric layer, significantly amplifying triboelectric charge generation (Figure 1b(iii)). The fabricated stretchable electrode PVA/H_3PO_4/MXene exhibits ultra-thin characteristics, conforming seamlessly to human skin (Figure 1c). Notably, fingerprints remained visible when the electrode was attached to the finger (Figure S2a, Supporting Information). After air plasma etching, the MXene-doped electrode solution fully wetted the Ecoflex surface, forming a robust bond capable of withstanding repeated stretching (Figure S2b, Supporting Information), ensuring long-term mechanical stability. Furthermore, the fabricated STS exhibits full twisting and stretching properties, with corresponding optical images shown in Figure 1d. Detailed fabrication procedures and selected materials are provided in the Experimental Section.

When the STS is adhered to human joints, the human skin acts as the positive triboelectric material, while the Ecoflex/MXene layer serves as the negative triboelectric material. As joints bend from the rest position (Figure S3a, Supporting Information), contact between the skin and Ecoflex/MXene induces electron cloud overlap at the interface. This overlap lowers the energy barrier for electron transfer, enabling triboelectric charge generation via contact electrification at the contact surface (Figure S3b, Supporting Information). The STS, strategically positioned at multiple joints to detect dynamic postures, generates electrical signals that are collected by a custom-designed multichannel data acquisition chip (process (i) in Figure 1e). This yields time-series datasets of joint bending angles for subsequent analysis. Data processing is implemented through two pathways: real-time threshold comparison (process (ii)) for immediate motion alerts and deep learning (process (iii)) for complex posture recognition, both illustrated in Figure 1e, ultimately enabling real-time movement monitoring and posture classification (process (iv)).

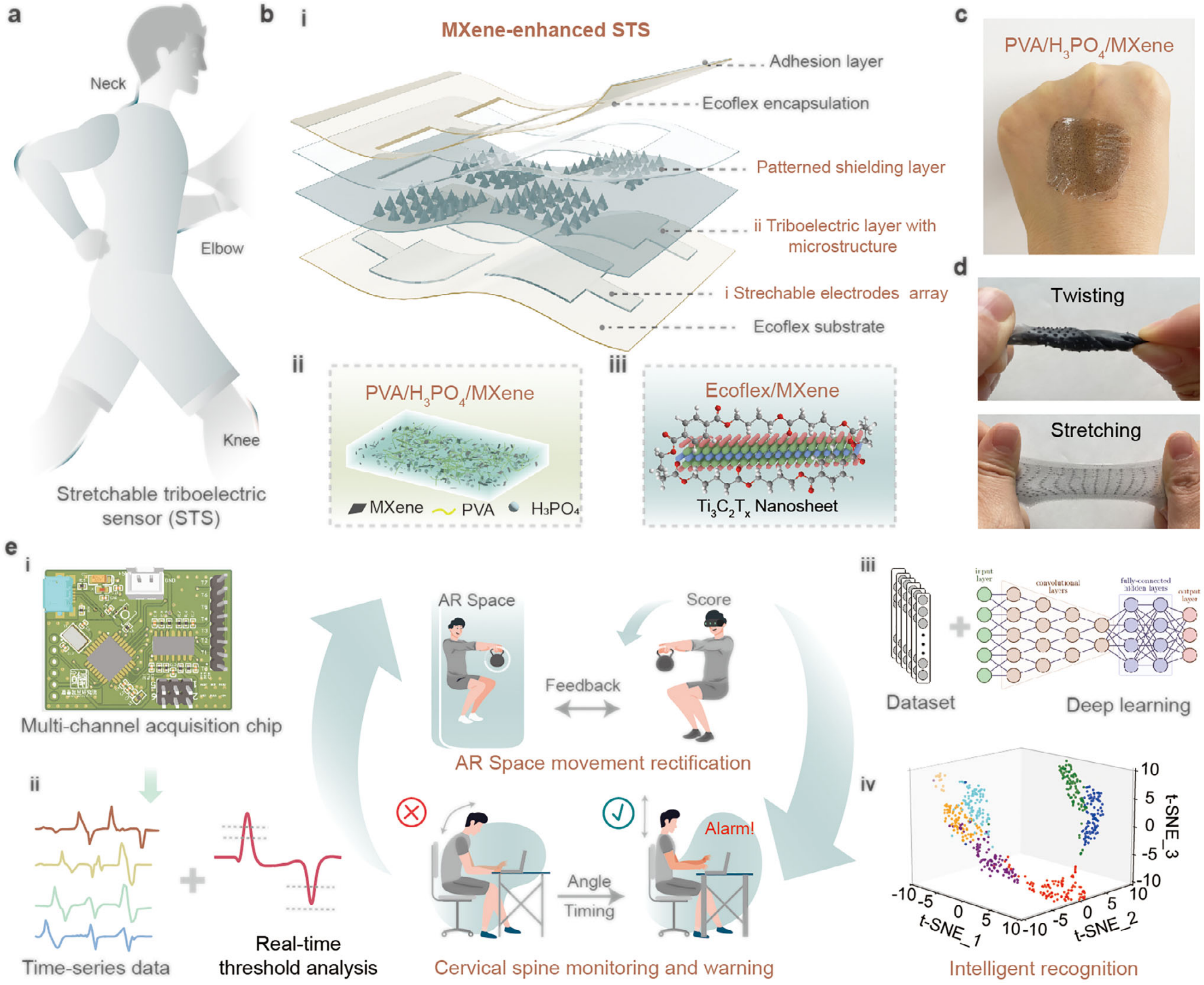

Figure 1. Design and mechanism of the wearable STS system. a) Concept diagram of a wearable STS system for motion recognition. b) Detailed structure and components of the MXene-enhanced STS. c) Photograph of PVA/H_3PO_4/MXene electrode. d) Photographs of the STS under twisting and stretching. e) Conceptual schematic diagram of intelligent motion recognition assisted by deep learning.

2.2. Electrical Performance and Sensing Characteristics of MXene-Enhanced STS

MXene possesses abundant surface functional groups (—OH, —F, —O, etc.) with negatively charged hydrophilic surfaces, enabling the formation of a 3D network with PVA via hydrogen bonding. Initially, various weight ratios (5%–30%) of H_3PO_4 to a 10 wt.% PVA solution were evaluated to determine the optimal ratio (Figure S4, Supporting Information). Considering improved stability and performance, a 20 wt.% H_3PO_4 concentration in the PVA solution was selected. Subsequently, MXene was doped into the PVA/H_3PO_4 electrode layer (EL) at weight ratios of 0.25, 0.5, 1, 1.5, and 2 wt.%. As depicted in **Figure** 2a, the output performance, including the voltage (*V*), current (*I*), and transferred charge (*Q*), was characterized, with corresponding curves provided in Figure S5 (Supporting Information). It can be observed that the addition of a small amount of MXene improves the output performance, with the maximum improvement observed at 0.5 wt.% MXene content: the *V* increased from 110 to 138 V. This enhancement is likely ascribed to microchannel formation and the electric double layer effect.[32] Under compression and release, contact electrification occurs at the interface between MXene and other molecules between these phases.[43] However, once the MXene content exceeds 0.5 wt.%, the performance declines due to nanosheet agglomeration, which hinders ion transport within the electrode layer.[43]

MXene is also incorporated into the stretchable triboelectric layer. As depicted in Figure 2b, the output performance peaks at 9 wt.% MXene loading, with *V* increasing from 110 to 165 V. Corresponding comparison data curves are shown in Figure S6 (Supporting Information). This enhancement is attributed to MXene's high negative triboelectric properties and strong electron affinity from abundant —F/—O functional groups.[30] Additionally, acting as a nanomaterial, MXene increases both the surface area of the Ecoflex and the effective surface contact area. However, when the MXene content exceeds 12 wt.%, the performance

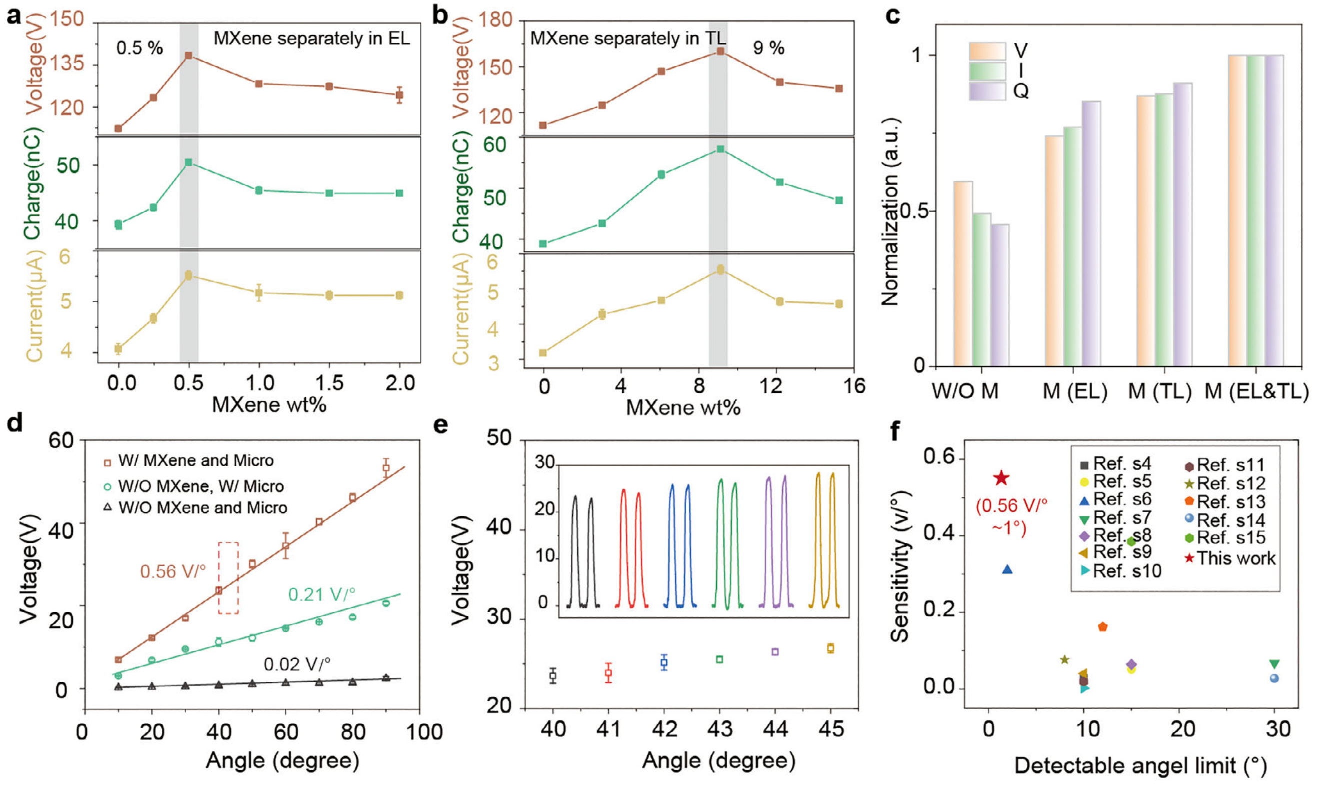

Figure 2. Electrical and sensing performance of MXene-enhanced STS.a,b) Electrical output characteristics (voltage, current, and transferred charge) of STS devices with a) varying MXene loadings in the electrode layer (EL) and b) triboelectric layer (TL). c) Normalized performance comparison among different STSs under MXene mixing scenarios. d) Sensitivity comparison of angle sensing of three types STSs. e) The voltage signal value varies in ≈1 ° increments within the 40–45° range. The inset shows the corresponding voltage curves. f) Comparison of the angle sensing sensitivity and resolution of the triboelectric angle sensors with other reported works.

shows a declining tendency due to the gradual accumulation of nanosheets. Furthermore, four STS configurations were systematically compared:1) without MXene (W/O M), 2) with MXene in the electrode layer only (M in EL), 3) with MXene in the triboelectric layer only (M in TL), 4) with MXene in both layers (M in EL & TL). The results in Figure 2c reveal a synergistic performance boost when MXene is added to both layers: V increases by 41% (110 V → 185 V), I by 51% (4.6 μA → 10.1 μA), and Q by 55% (32 nC → 65 nC) under identical contact-separation testing conditions.

To quantitatively evaluate the sensing performance, the MXene-enhanced STS was attached to the finger for angle monitoring. For a self-powered triboelectric sensor, the air gap or microstructure is a key component.[22,44] Three STS configurations were systematically evaluated: 1) without MXene and microstructure (W/O MXene and Micro), 2) with microstructure but without MXene (W/O MXene, W/ Micro), 3) with both MXene and microstructure (W/ MXene and Micro). As shown in Figure 2d, the sensitivity was effectively enhanced from 0.02 V/° (W/O MXene and Micro) to 0.21 V/° (W/O MXene, W/Micro) due to the presence of the microstructures (Figure S7, Supporting Information). Further incorporation of MXene boosted sensitivity to 0.56 V/° with excellent linearity (R^2 = 0.99) across the 0–90° bending range, representing a 167% improvement over the microstructure-only device. The bending range was constrained by finger joint mechanics. Notably, the enhanced STS achieved a 1° sensing resolution, demonstrated by gradual finger bending in 1° increments from 40° to 45°, with distinct voltage responses shown in Figure 2e. The inset curves confirm clear differentiation of ≈1° angle changes. A comparative analysis with state-of-the-art triboelectric angle sensors is summarized in Table S1 (Supporting Information). As shown in Figure 2f, the STS outperforms most reported sensors in sensitivity (0.56 V/°), resolution (1°), and softness, highlighting its competitive edge in wearable applications. Additionally, the STS demonstrated robust external force sensing (4–40 N) with stable responses at each force level, as shown in Figure S8 (Supporting Information).

2.3. Sensing Mechanism and Performance of the STS

To elucidate the sensing mechanism for different external stimuli, a simplified schematic and finite element simulations of the STS's electric potential distribution during bending or pressing are shown in **Figure** 3a–c. The Ecoflex/MXene exhibits triboelectric electronegativity while the skin tends to lose electrons. The model was configured under open-circuit conditions, with the simulated output voltage defined as zero when the interface surfaces of the two materials first make contact (Δh = 0 mm), which was the same as the measurement setup. Under external bending

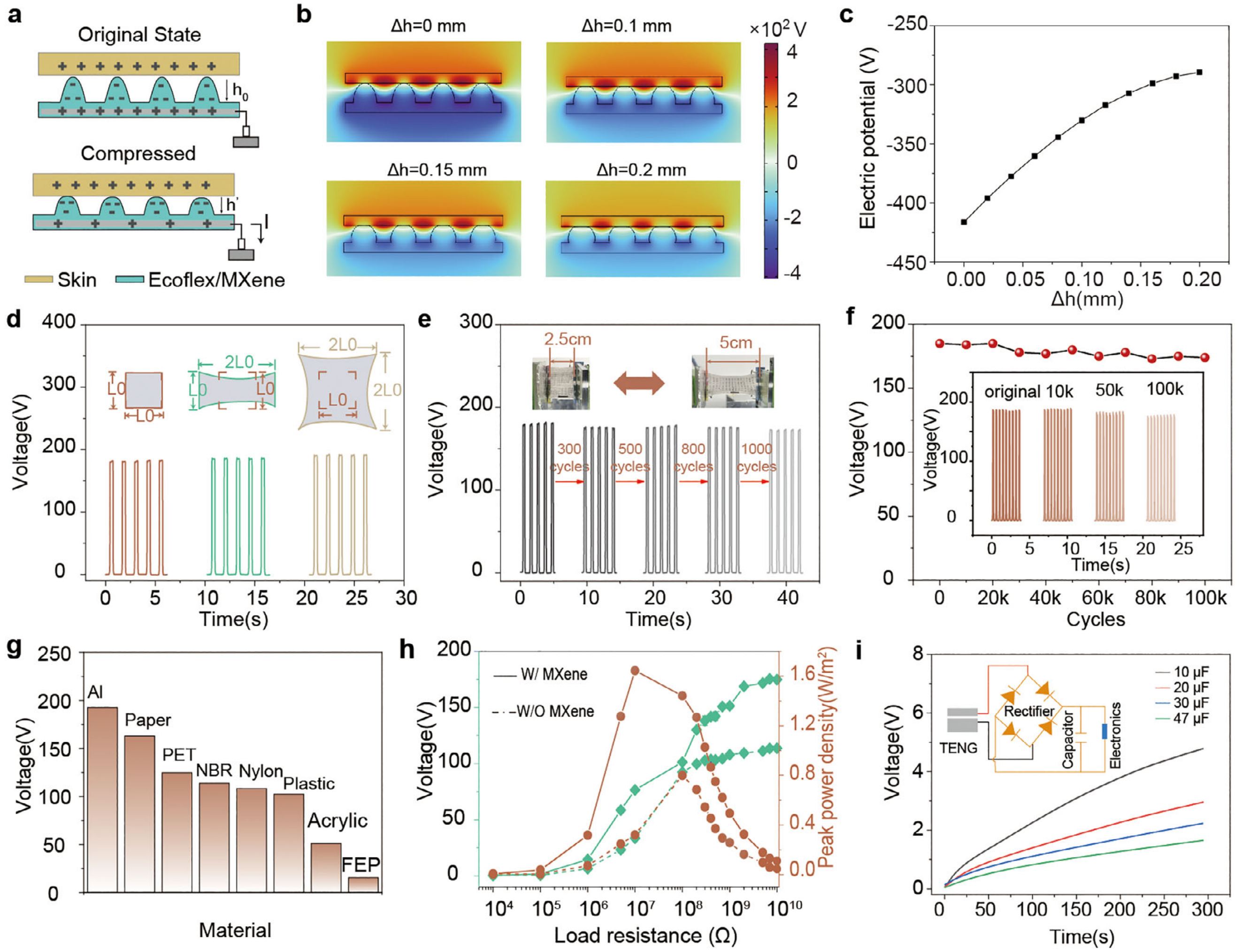

Figure 3. Sensing mechanism and mechanical-electrical performance of the MXene-enhanced STS. a–c) Triboelectric mechanism and simulated electric potential distribution at different deformation depths. d) STS's voltage responses to periodic uniaxial and biaxial elongation at 100% strain. e) Voltage stability after 300, 500, 800, and 1000 cycles of 100% strain uniaxial stretching. f) Long-term durability under 50 N cyclic loading for 100000 cycles. g) Voltage outputs with different triboelectric contact materials. h) Voltage, current, and output power of STS with/without MXene versus external load resistance. i) Charging curves of 10–47 μF capacitors by the STS under consistent working frequency.

or pressure, the microstructure is gradually compressed, causing the electric potential of the embedded STS electrode to increase and the simulated outputs to rise, thus aligning with the trend of actual sensing results.

Stretchability is a critical parameter for conformable joint sensing. The STS's ability to conform to complex joint movements enables accurate angle perception. As depicted in Figure 3d, the STS was subjected to periodic uniaxial and biaxial elongation tests at 100% strain, with corresponding test images provided (Figure S9, Supporting Information). These tests were carried out using a linear motor setup, with aluminum (Al) serving as the other contact object. The results indicate that the STS maintains a stable output voltage of ≈185 V. Although the 100% elongation increases the triboelectric area in the contact-separation mode, the conductive performance of the MXene/PVA/H_3PO_4 film decreases under stretching, leading to an overall stable output due to offsetting effects. This confirms that the STS functions reliably under both uniaxial and biaxial deformation. To evaluate cyclic durability further, the STS was subjected to uniaxial stretching at 100% strain for 300, 500, 800, and 1000 cycles, with voltage output measured in the relaxed state after each cycle (Figure 3e). The results demonstrate consistent performance, with only a slight voltage decrease from 185 to 178 V after 1000 cycles. Additionally, long-term stability was assessed under 100000 cycles of linear motor-driven loading (≈50 N), as shown in Figure 3f. The STS exhibited negligible performance degradation, thereby validating the robustness of the solid-state polymer electrode and overall device integrity.

Contact-separation tests with various materials (Figure 3g) showed that aluminum—with its high positive triboelectric polarity—yielded the highest output, justifying its use as the counter material in most electrical signal tests. Notably, when tested with fluorinated ethylene propylene (FEP), the MXene-enhanced STS still generated a positive voltage of 16 V, confirming that the Ecoflex/MXene triboelectric layer exhibits stronger electronegativity than FEP. This test demonstrates the STS's ability to discriminate between materials. Energy harvesting performance was evaluated by measuring voltage, current, and output power of the STS with and without MXene under varying external resistances (Figure 3h). The MXene-enhanced STS achieved an output power of 1.6 W m^{-2}—twice that of the STS without MXene (0.8 W m^{-2})—with a reduced optimal matching resistance from 100 to 10 MΩ. These results indicate that MXene doping enhances both sensing characteristics and energy conversion efficiency. Practical applications were demonstrated by a single STS lighting up 48 series-connected LED displays forming the characters "JSFD" (Figure S10a, Supporting Information). Additionally, a single STS has the capacity to charge a variety of capacitors after a rectifier, namely 10, 20, 30, and 47 μF capacitors. A larger capacitance value stores more electric charge and results in a slower charging speed, as presented in Figure 3i. It takes only 260 s to charge a 47 μF capacitor to 1.5 V, and the stored electric charge can power a timer (Figure S10b, Supporting Information). MXene's synergistic enhancement across functional layers improves the STS's angle sensing performance and reduces energy harvesters' internal resistance, offering new insights for multifunctional layer synergistic design in the field. It validates cross-functional material synergy, advances integrated devices toward high performance and practicality, and lays the groundwork for technological breakthroughs and application expansion.

2.4. Fitness Monitoring and Posture Adjustment with AR Interface

Overall, the MXene-enhanced STS achieves a high angular sensitivity of 0.56 V/° and a resolution of ≈1°, coupled with excellent long-term stability over 100,000 cycles. These key properties—enabling precise capture of subtle joint angle changes and consistent signal output even after prolonged use—lay a critical foundation for reliable real-time posture monitoring, which is essential for the accuracy and robustness of AR-assisted feedback systems. Building on this, a real-time monitoring of joint bending dynamics was achieved by attaching the STS to multiple human joints, allowing accurate tracking of diverse movements and postures. First, precise acquisition of multi-channel triboelectric sensor data was critical. A pre-processed circuit (PPC) was designed to condition the high-impedance triboelectric signal, as described in Figure S11a (Supporting Information). The crosstalk between multi-channel signals can be significantly reduced with the PPC design (Figure S11b, Supporting Information). The STS was then mounted on the elbow, knee, and waist to monitor joint bending angles using the multi-channel data acquisition system (Figure S12, Supporting Information). A fitness virtual interface was developed by Unity. As illustrated in **Figure** 4a, the STS's data are processed by the PPC before being transmitted to the Arduino Mega ADC. Data were then wirelessly sent to a computer via Bluetooth to integrate with an augmented reality (AR) interface equipped with a camera, enabling real-time synchronization between physical movements and virtual avatars. The AR system provides exercise guidance by analyzing joint angle signals in real time, offering feedback through threshold-based evaluations on the virtual interface. This feature enables repeated adjustments until the movement exactly matches the predefined action. As shown in Figure 4b, the virtual avatar issues a fitness command to "bend the arm vertically". Initially, insufficient bending (signal peaks below the preset threshold) triggers the feedback "Not good," prompting the user to increase flexion. As the bending angle meets the target, the evaluation updates to "Nice" and finally "Perfect" when the vertical angle is precisely achieved (Video S1, Supporting Information). Consistently, the experimental validations based on the AR-assisted feedback system were performed on leg bending (Figure S13, Supporting Information). By leveraging the wearable STS and AR system, we enable real-time fitness monitoring and immediate feedback to facilitate continuous posture adjustment, highlighting the potential of virtual interface-assisted rehabilitation.

For complex posture recognition—especially when handling multi-channel sensor data—a single threshold evaluation system is insufficient. Five STS sensors were positioned on the arms, legs, and waist to monitor six postures: bending pose, chair pose (C—P), tree pose (T—P), eagle pose (EA—P), elbow-leg pose (EL—P), and elbow pose (E—P), as depicted in Figure 4c. Leveraging deep learning—a key technology in artificial intelligence that mimics neural network operations—complex multi-channel data were efficiently processed. As illustrated in Figure 4d, a 1D-CNN model structure comprising four convolutional layers and two fully connected layers was employed. For each posture, five-channel STS data were sequentially concatenated into samples with 352 feature values. With 100 samples per posture, the input dataset comprised 600 × 352 features. As shown in Figure 4e(i), after directly applying t-distributed stochastic neighbor embedding (t-SNE) for dimensionality reduction, the feature distribution of the six samples appeared relatively scattered. By contrast, t-SNE of CNN-processed features (Figure 4e(ii)) revealed distinct inter-class boundaries and tight intra-class clustering, demonstrating the model's ability to extract discriminative features. After 50 epochs of training (Figure S14, Supporting Information), the model converged, achieving 97.3% accuracy in recognizing the six postures on the validation dataset (Figure 4f). These results highlight the utility of deep learning for intelligent recognition of complex postures, facilitating accurate replication of AR-guided movements.

2.5. Intelligent Recognition of Cervical Spine Posture

In information-driven workplaces, prolonged static postures often induce cervical spine biomechanical imbalance, a primary cause of sub-health among employees. Persistent abnormal curvature can lead to irreversible damage, including muscle strain, cervicogenic headaches, and degenerative cervical diseases, underscoring the need for real-time posture monitoring and early feedback for adjustment. Single sensors can only detect simple joint bending/extension, necessitating a sensor array to recognize complex cervical movements like head bowing, turning, and tilting. This study presents a 2 × 2 cross-shaped stretchable triboelectric sensor array (STSA) for cervical posture recognition, with the optical images shown in Figure S15 (Supporting Information). A patterned shielding layer (PSL) of PVA/H_3PO_4 above the triboelectric layer—connected to the data acquisition board's GND port—mitigates crosstalk from non-sensing regions, as

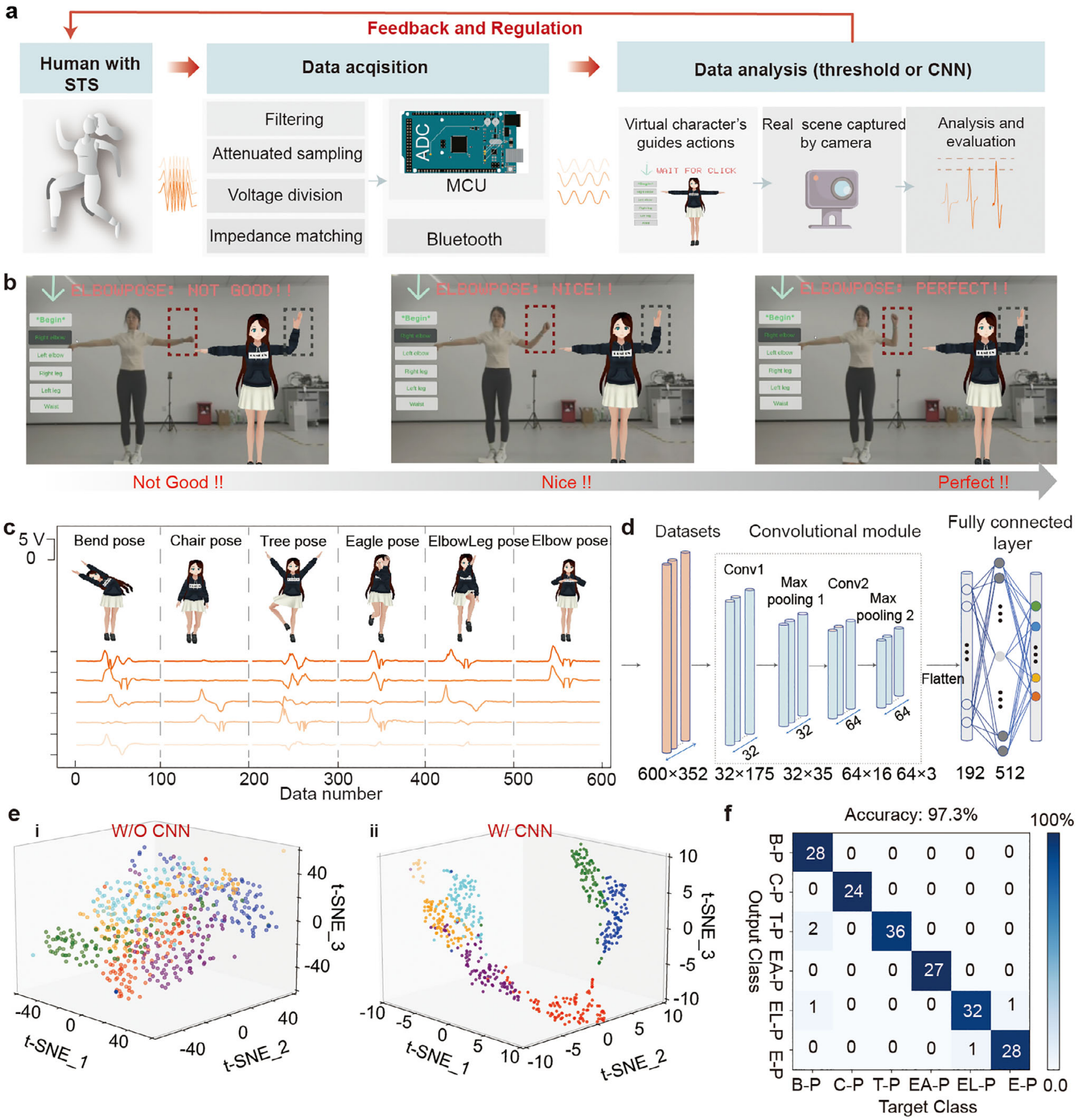

Output Class \ Target Class	B-P	C-P	T-P	EA-P	EL-P	E-P
B-P	28	0	0	0	0	0
C-P	0	24	0	0	0	0
T-P	2	0	36	0	0	0
EA-P	0	0	0	27	0	0
EL-P	1	0	0	0	32	1
E-P	0	0	0	0	1	28

Figure 4. Real-time posture analysis and feedback via the STS-AR system. a) Schematic of motion monitoring and posture adjustment on an AR interface (sensing-collection-analysis-feedback). b) Posture assessment and adjustment process until alignment with a virtual character's predefined action. c) Output voltage signal of the five channels during six kinds postures. d) Architecture of the 1D-CNN model for posture recognition. e) 2D feature distributions via t-SNE dimensionality reduction for i) original raw and ii) CNN-processed datasets. f) Confusion matrix of six posture by trained CNN model on test datasets.

illustrated in **Figure** 5a. Electrical signals were compared across three configurations: without shield (W/O PSL), with shield (W/ PSL), and with shield plus encapsulation layer (W/ PSL & EL) (Figure 5b). Notably, gentle non-sensing site contact i) induced significant interference in W/O PSL, whereas W/ PSL and W/ PSL & EL showed negligible signals in sensing units ii, iii). When touching sensing units individually, W/ PSL exhibited no crosstalk, while W/O PSL showed residual interference. Considering that the solid-state polymer PVA/H_3PO_4 is still capable of absorbing moisture and becoming unstable when exposed to air over a long time, a thin Ecoflex layer was applied for encapsulation to ensure long-term operational stability of the device.

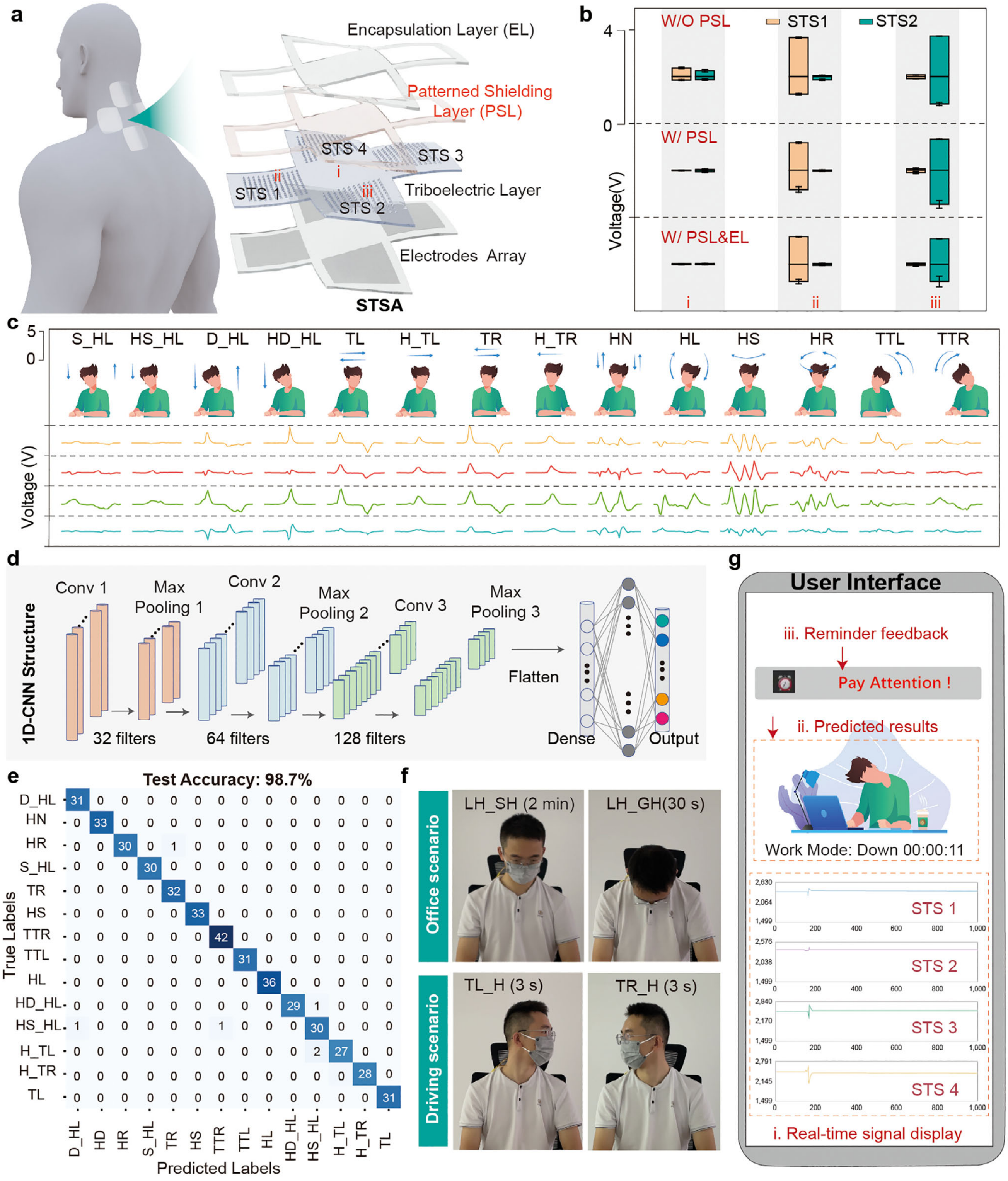

Figure 5. Deep learning-empowered intelligent recognition with the STSA system. a) Structure of the cross-shaped sensor array with a patterned shielding layer. b) Comparison of electrical signals from sensing units (ii, iii) and non-sensing unit (i) across three configurations: without shield (W/O PSL), with shield (W/ PSL), and with shield plus encapsulation layer (W/ PSL & EL). c) Output voltage signal of the STSA for 14 cervical spine postures. d) Architecture of 1D-CNN model for decoding 14 cervical spine postures. e) Confusion matrix of the trained CNN model on the test dataset, achieving 98.7% accuracy. f) Photographs and workflow of real-time intelligent recognition in office and driving scenarios. g) Smartphone interface for intelligent recognition, including i) real-time signal display, ii) predictions from the trained CNN, iii) feedback reminder.

The W/ PSL & EL configuration minimized both interference and crosstalk. To validate scalability, a 3 × 3 STSA with/without shielding was fabricated (Figure S16, Supporting Information), yielding consistent results during sliding tests (Figure S17, Supporting Information). As schematized in Figure S18 (Supporting Information), the shield redirects non-sensing site charges to GND, preventing cross-induction in sensing units. Collectively, these results demonstrate that the STSA with patterned shielding and encapsulation enhances signal fidelity, providing high-quality data for deep learning-driven cervical posture recognition.

The above results demonstrate that the STSA equipped with a PSL can effectively suppress signal crosstalk in non-sensing regions. Four-channel sensing units can accurately capture the characteristic signals of subtle and complex cervical spine movements, outputting high-fidelity time-series data. Thus, fourteen head postures were intelligently recognized via deep learning, including: slight head lowering (S_HL, head tilting downward by ≈10°–20° from neutral position), half-cycle slight head lowering (HS_HL, initiating slight head lowering without returning to neutral position), deep head lowering (D_HL, head tilting downward by ≈30°–45° from neutral position), half-cycle deep head lowering (HD_HL, initiating deep head lowering without returning to neutral position), head turning left (TL, head rotating left from front-facing position and returning to neutral position), half-cycle head turning left (H_TL, initiating left rotation without returning to front-facing position), head turning right (TR, head rotating right from front-facing position and returning to neutral position), half-cycle head turning right (H_TR, initiating right rotation without returning to front-facing position), head nodding (HN, repeated up-down movement of the head with full return to neutral between cycles), head lifting (HL, head tilting upward from neutral position), head shaking (HS, repeated left-right rotation with full return to neutral between cycles), head rotating (HR, 360° circular rotation of the head), head tilting left (TTL, head inclining leftward such that the left ear approaches the left shoulder), and head tilting right (TTR, head inclining rightward such that the right ear approaches the right shoulder), with specific postural movements shown in Figure 5c. Here, "half-cycle" specifically refers to an incomplete movement that stops at the midpoint of the action without resetting to the initial neutral position. All abbreviations in this work are listed in Table S2 (Supporting Information). A 1D-CNN, whose corresponding PyTorch code is presented in Figure S19a (Supporting Information), includes three convolutional layers with 32, 64, and 128 filters, alternating with max pooling layers. A fully connected layer outputs a 14-dimensional classification result, with the schematic diagram shown in Figure 5d. After 100 epochs of training, the model achieved convergence with stable loss, as evidenced by the training and test accuracy curves and loss curves depicted in Figure S19b (Supporting Information). The model's confusion matrix for the test dataset demonstrated an overall recognition accuracy of 98.7%, as illustrated in Figure 5e. To enable real-time inference, the trained model was deployed to the mobile terminal, with the logic flowchart of training phase and real-time prediction shown in Figure S20 (Supporting Information).

To enable real-time mobile recognition, the PyTorch model was converted to TorchScript and deployed to a mobile app (Figure S21, Supporting Information). Two early-warning scenarios were demonstrated: 1) Office cervical health monitoring: The app tracked half-cycle slight head lowering (HS_HL, threshold: 2 min) and half-cycle deep head lowering (HD_HL, 30 s); 2) Simulated driving safety: Half-cycle head turning left (H_TL) and right (H_TR) were monitored with a 3 s threshold for alerting (Figure 5f). As illustrated in Figure 5g, real-time STSA data are processed by the trained CNN for intelligent prediction, triggering a countdown timer based on the predicted results. When postures exceed thresholds, multimodal alerts (sound and pop-ups) activate (Video S2, Supporting Information). This prototype demonstration indicates that the sensing chain comprising wearable sensing devices, deep learning-based intelligent recognition, and closed-loop feedback establishes a new paradigm for future proactive health monitoring, while also validating the effectiveness of the hardware-algorithm co-optimization strategy in wearable medical electronics.

3. Conclusion

In summary, we developed a self-powered stretchable triboelectric sensor (STS) system for intelligent posture recognition via deep learning. MXene ($Ti_3C_2T_x$) nanosheets were integrated into functional layers to enhance the STS's output performance, thereby boosting its sensing capabilities. The optimized STS exhibits a high angle sensitivity of 0.56 V/° and an angular resolution of ≈1°, enabling precise tracking of human limb bending angles. The STS exhibits excellent stability over 100000 cycles due to the robustness of the solid-state polymer electrode film. These features collectively enable precise tracking and evaluation of joint dynamics, with real-time feedback provided until postures align with standard movements. Furthermore, aiming at the monitoring of complex cervical spine postures, an STSA featuring an additional patterned film shielding layer was fabricated to function as a sensing unit. A 1D-CNN model was utilized to achieve 98.7% accuracy in identifying 14 postures from 4-channel triboelectric signals. Additionally, a mobile terminal deployed with the trained CNN enables real-time intelligent predictions and multi-modal feedback (e.g., sound alerts). This study presents a novel paradigm for intelligent wearable systems in proactive health management and posture correction, combining self-powered sensing, deep learning, and mobile technology to address occupational health challenges.

4. Experimental Section

Preparation of Functional Layers of the Device: i) Preparation of PVA/H_3PO_4 Electrode: Polyvinyl alcohol (PVA, MW 89000–98000, >99% hydrolyzed, Sigma-Aldrich) was dissolved in deionized water at 90 °C under constant stirring for 2 h to form a homogeneous 10 wt.% solution. Subsequently, phosphoric acid (H_3PO_4, 85%, Sigma-Aldrich) was added to the PVA solution at mass ratios of 5%, 10%, 20%, and 30%. The mixture was stirred at 500 rpm for 1 h to yield a uniform PVA/H_3PO_4 gel. ii) Preparation of Composite Electrode Film (PVA/H_3PO_4/MXene): Commercially purchased MXene ($Ti_3C_2T_x$) powder was incorporated into the PVA/H_3PO_4 gel at mass fractions of 0.25, 0.5, 1, 1.5, and 2 wt.%. Uniform dispersion was achieved via ultrasonic treatment (SUV-5K, 40 kHz, 10 min) followed by mechanical stirring (IKA C-MAG, 50 rpm, 10 min). Subsequently, the solution was left to stand for 24 h to allow bubbles to dissipate, resulting in MXene/PVA/H_3PO_4 gel systems with varying mass ratios. iii) Preparation of MXene/Ecoflex Triboelectric Layer (MXene/Ecoflex): The A:B components of Ecoflex 0030 silicone rubber were mixed at a mass ratio of 1:1

and stirred for 2 min to achieve a homogeneous silicone rubber. MXene powder was added at mass ratios of 3, 6, 9, 12, and 15 wt.%, followed by vacuum degassing at 60 °C for 30 min to remove entrapped air, forming MXene/Ecoflex composites.

Fabrication Process of the Device: i) Single STS Fabrication: A 3D mold featuring a pyramidal microstructure (dimensions of $700 \times 700 \times 700$ µm) with an effective working area of 2×2 cm^2 was created. Then, the MXene/Ecoflex mixture was first poured into the mold to form the triboelectric layer of the device, followed by curing in a vacuum drying oven at 60 °C for 2 h. Next, the surface of the triboelectric layer was treated by RIE ion etching (air plasma, 60 W, 30 s) to obtain a hydrophobic-to-hydrophilic transition. Then, a certain mass (5 mg cm^{-2}) of the MXene/PVA/H_3PO_4 mixed gel was coated on the surface of the modified triboelectric layer as the electrode. After embedding a copper wire, the structure was vacuum-dried at 40 °C for 24 h to form a stretchable ultra-thin solid-state electrode film. Finally, an Ecoflex encapsulation layer was applied, and the device was cured at 60 °C for 2 h before carefully demolding the 3D structure. ii) STSA with Shielding Layer: A patterned PET mask featuring a "sensing array" was fabricated using a CO_2 laser engraving machine (KT-4060 100 W). A 3D-printed mold with a "cross"-shaped array structure and integrated shielding layer was prepared via computer-aided design (3D Max). First, Ecoflex silicone rubber was poured into the non-sensing areas of the mold to form the outermost patterned encapsulation layer according to the array design. The Ecoflex surface in non-sensing regions was treated with reactive ion etching (RIE, 60 W, 30 s), followed by spin-coating a PVA/H_3PO_4 electrode to serve as the patterned shielding layer. Next, the MXene/Ecoflex mixture was poured into the mold to form the triboelectric layer, which was cured in a vacuum oven at 60 °C for 2 h and subjected to RIE treatment. The PVA/H_3PO_4/MXene electrode array was defined using the PET mask, after which the mask was removed. Finally, a thin Ecoflex encapsulation layer was applied to complete the array device.

Neural Network Training: The dataset was gathered using the developed multi-channel data acquisition chip. Data were sampled every 2 s and recorded for at least 100 repetitions per posture. The training and test datasets were divided at a 7:3 ratio. A model was built using the PyCharm platform and PyTorch framework (Python 3.9), with raw data normalized prior to training. During optimization, hyperparameters—including learning rate, epoch count, activation function, optimizer, and batch size—were systematically tuned. The Adam optimizer and Cross-Entropy Loss were employed throughout training, with experiments conducted on a computer equipped with an NVIDIA GeForce GTX 1660 SUPER GPU.

Posture Adjustment and Intelligent Recognition: i) Posture Adjustment: A STS device was attached to three key joints of the human body, aligned with the joints' core movement axes to ensure accurate angle acquisition. Elbow: Centered ≈1–2 cm above the elbow crease, matching the movement trajectory of the humeroulnar joint; Knee: ≈1–2 cm directly above the patella apex, capturing the flexion movement of the knee joint; Waist: Positioned ≈2 cm lateral to the spinous process of the L4–L5 vertebrae, monitoring the lateral flexion and forward flexion angles of the waist. The target skin area was wiped in a circular motion with 75% medical ethanol for 10 s, then air-dried naturally for 30 s to remove surface oil and impurities. 3 M Transpore medical transparent tape was used to fix two opposite edges of the STS, leaving the other two edges free to prevent from restricting joint movement while maintaining partial breathability. After the STS devices were properly attached (as described above), AR was implemented via Unity, with the experimental setup equipped with a commercial camera—this enabled real-time synchronization between the participant's physical movements and virtual avatars. ii) Intelligent Recognition:For cervical posture monitoring, the cross-shaped STSA (Figure S15, Supporting Information) was centrally attached to the midline of the posterior neck. The cross intersection was positioned using the hyoid bone as a marker, accurately aligned with the C4-C5 vertebral level—this ensured coverage of the cervical spine's core movement area, thereby providing stable signals for the recognition of 14 cervical postures. The smartphone application was developed using Android Studio with Java, targeting Android 12 and above. The trained 1D-CNN model was converted to TorchScript format and integrated into the app. The app architecture supports real-time data streaming from the STS array, dynamic posture prediction using the embedded CNN, and configurable alerts with sound notifications and visual prompts. Experimental results demonstrate 98.7% recognition accuracy on mobile devices, validating the system's feasibility for on-the-go cervical health monitoring. In the test, the STS and STSA used for posture monitoring were attached to the surface of human skin, with the devices secured using commercial medical transparent tape. This experimental operation caused no physical harm to the human body; after the experiments, no adverse effects (either physical or psychological) were observed in the volunteers.

Performance Characterization: A programmable electrometer (Keithley 6514) was used to test the electrical properties of the device (including short-circuit current (*I*), open-circuit voltage (*V*), and transferred charge (*Q*)). A stepping motor (LinMot, X12BC) was used to apply normal pressure to the devices. A scanning electron microscope (Nova NanoSEM 450 and SU1510 Hitachi) was used to evaluate the microstructure. The application part, the self-developed data acquisition board, and Arduino platform were utilized to obtain multi-channel electrical signals from the device, and a software platform was constructed based on the PyQt framework.

Ethical Compliance: This study conducts non-invasive human posture monitoring using self-powered STS and STSA. These devices only adhere to the skin without invasive operations, tissue sampling, or risky interventions. Per the ethical guidelines of affiliated institutions, this experiment does not require IRB approval. A participant-specific informed consent form has been prepared, outlining the study purpose, sensor attachment, data scope, and participant rights. All participants will sign the form before participation, with signed copies archived.

Supporting Information

Supporting Information is available from the Wiley Online Library or from the author.

Acknowledgements

J.T. and J.H. contributed equally to this work. The authors thank the National Natural Science Foundation of China (Nos. 61874029, 52192610, 62422120, 52371202, 52125205, and 52250398), Natural Science Foundation of Beijing Municipality (L223006), Shenzhen Science and Technology Program (Grant No. KQTD20170810105439418) and the Fundamental Research Funds for the Central Universities.

Conflict of Interest

The authors declare no conflict of interest.

Data Availability Statement

The data that support the findings of this study are available from the corresponding author upon reasonable request.

Keywords

angle sensing, deep learning, posture monitoring, self-powered sensing, stretchability

Received: June 16, 2025
Revised: September 11, 2025
Published online:

---

[1] Y. Hong, B. Wang, W. K. Lin, L. H. Jin, S. Y. Liu, X. W. Luo, J. Pan, W. P. Wang, Z. B. Yang, *Sci. Adv.* **2021**, *7*, abf0795.

[2] S. S. An, X. J. Pu, S. Y. Zhou, Y. H. Wu, G. Li, P. C. Xing, Y. S. Zhang, C. G. Hu, *ACS Nano* **2022**, *16*, 9359.

[3] A. Z. Rao, S. S. Siddique, M. D. Mujib, M. A. Hasan, A. O. Alokaily, T. Tahira, *Ieee Access* **2024**, *12*, 41676.

[4] C. Y. Li, D. Liu, C. Q. Xu, Z. M. Wang, S. Shu, Z. R. Sun, W. Tang, Z. L. Wang, *Nat. Commun.* **2021**, *12*, 11846.

[5] M. Nankali, M. A. Amindehghan, S. H. S. Alagheband, A. M. Shahtoori, R. Seethaler, N. M. Nouri, A. S. Milani, *Adv. Mater. Technol.* **2024**, *9*, 2400071.

[6] Y. P. Li, S. J. Tan, L. Y. Yang, L. Y. Li, F. Fang, Q. Z. Sun, *Adv. Fiber Mater.* **2022**, *4*, 226.

[7] R. R. Bao, J. Tao, J. Zhao, M. Dong, J. Li, C. F. Pan, *Sci. Bull.* **2023**, *68*, 1027.

[8] J. Tao, M. Dong, L. Li, C. Wang, J. Li, Y. Liu, R. Bao, C. Pan, *Microsyst. Nanoeng.* **2020**, *6*, 62.

[9] G. Wu, X. Li, R. Bao, C. Pan, *Adv. Funct. Mater.* **2024**, *34*, 2405722.

[10] H. C. Xu, Y. Liu, Y. P. Mo, Z. Y. Chen, X. J. Pan, R. R. Bao, C. F. Pan, *Rare Met.* **2025**, *44*, 4839.

[11] F. Lorestani, X. Zhang, A. M. Abdullah, X. Xin, Y. Liu, M. M. Rahman, M. A. S. Biswas, B. Li, A. Dutta, Z. Niu, S. Das, S. Barai, K. Wang, H. Cheng, *Adv. Funct. Mater.* **2023**, *33*, 2306117.

[12] Z. K. Li, S. M. Zhang, Y. H. Chen, H. N. Ling, L. B. Zhao, G. X. Luo, X. C. Wang, M. C. Hartel, H. Liu, Y. M. Xue, R. Haghniaz, K. Lee, W. J. Sun, H. Kim, J. Lee, Y. C. Zhao, Y. P. Zhao, S. Emaminejad, S. Ahadian, N. Ashammakhi, M. R. Dokmeci, Z. D. Jiang, A. Khademhosseini, *Adv. Funct. Mater.* **2020**, *30*, 2003601.

[13] Y. Chang, L. Wang, R. Y. Li, Z. C. Zhang, Q. Wang, J. L. Yang, C. F. Guo, T. R. Pan, *Adv. Mater.* **2021**, *33*, 2003464.

[14] R. H. Han, Y. Liu, Y. P. Mo, H. C. Xu, Z. W. Yang, R. R. Bao, C. F. Pan, *Adv. Funct. Mater.* **2023**, *33*, 2305531.

[15] C. P. Jiang, W. Q. Xu, Y. T. Li, Z. J. Yu, L. C. Wang, X. T. Hu, Z. Y. Xie, Q. K. Liu, B. Yang, X. L. Wang, W. X. Du, T. T. Tang, D. Z. Zheng, S. Q. Yao, C. W. Lu, J. Q. Liu, *Nat. Commun.* **2024**, *15*, 9513.

[16] Y. Liu, J. Tao, Y. P. Mo, R. R. Bao, C. F. Pan, *Adv. Mater.* **2024**, *36*, 2313857.

[17] C. A. Petroff, G. Cassone, J. Sponer, G. R. Hutchison, *Adv. Mater.* **2021**, *33*, 2007486.

[18] J. Tao, R. R. Bao, X. D. Wang, Y. Y. Peng, J. Li, S. Fu, C. F. Pan, Z. L. Wang, *Adv. Funct. Mater.* **2019**, *29*, 1806379.

[19] H. Y. Zou, Y. Zhang, L. T. Guo, P. H. Wang, X. He, G. Z. Dai, H. W. Zheng, C. Y. Chen, A. C. Wang, C. Xu, Z. L. Wang, *Nat. Commun.* **2019**, *10*, 1427.

[20] Z. J. Li, S. X. Zhang, H. Y. Guo, B. Wang, Y. Gong, S. Y. Zhong, Y. Peng, J. Y. Zheng, X. H. Xiao, *Nano Energy* **2023**, *113*, 108595.

[21] C. Y. Wang, H. Y. Guo, P. Wang, J. W. Li, Y. H. Sun, D. Zhang, *Adv. Mater.* **2023**, *35*, 2209895.

[22] Z. L. Wang, *Adv. Energy Mater.* **2020**, *10*, 2000137.

[23] Q. Zheng, L. Xin, Q. Zhang, F. Shen, X. Lu, C. Cao, C. Xin, Y. Zhao, H. Liu, Y. Peng, J. Luo, H. Guo, Z. Li, *Adv. Mater.* **2025**, *37*, 2417380.

[24] B. B. Shao, M. H. Lu, T. C. Wu, W. C. Peng, T. Y. Ko, Y. C. Hsiao, J. Y. Chen, B. Q. Sun, R. Y. Liu, Y. C. Lai, *Nat. Commun.* **2024**, *15*, 1238.

[25] C. Zhang, H. M. Chen, X. H. Ding, F. Lorestani, C. L. Huang, B. W. Zhang, B. Zheng, J. Wang, H. Y. Cheng, Y. Xu, *Appl. Phys. Rev.* **2022**, *9*, 011413.

[26] J. N. Kim, J. Lee, T. W. Go, A. Rajabi-Abhari, M. Mahato, J. Y. Park, H. Lee, I. K. Oh, *Nano Energy* **2020**, *75*, 104904.

[27] Y. H. Wang, L. Chu, S. Meng, M. X. Yang, Y. D. Yu, X. K. Deng, C. Qi, T. T. Kong, Z. Liu, *Adv. Sci.* **2024**, *11*, 2401436.

[28] T. Jin, Z. D. Sun, L. Li, Q. Zhang, M. L. Zhu, Z. X. Zhang, G. J. Yuan, T. Chen, Y. Z. Tian, X. Y. Hou, C. Lee, *Nat. Commun.* **2020**, *11*, 5381.

[29] R. Cao, X. J. Pu, X. Y. Du, W. Yang, J. N. Wang, H. Y. Guo, S. Y. Zhao, Z. Q. Yuan, C. Zhang, C. J. Li, Z. L. Wang, *ACS Nano* **2018**, *12*, 5190.

[30] M. Salauddin, S. M. S. Rana, M. Sharifuzzaman, M. T. Rahman, C. Park, H. Cho, P. Maharjan, T. Bhatta, J. Y. Park, *Adv. Energy Mater.* **2021**, *11*, 2002832.

[31] B. B. Shao, T. C. Lu, M. H. Lu, Y. T. Chen, T. C. Wu, W. C. Peng, T. Y. Ko, J. Y. Chen, B. Q. Sun, C. Y. Chen, R. Y. Liu, F. C. Hsu, Y. C. Lai, *Adv. Mater.* **2024**, *36*, 2408936.

[32] X. X. Luo, L. P. Zhu, Y. C. Wang, J. Y. Li, J. J. Nie, Z. L. Wang, *Adv. Funct. Mater.* **2021**, *31*, 2104928.

[33] C. Cao, Z. Li, F. Shen, Q. Zhang, Y. Gong, H. Guo, Y. Peng, Z. L. Wang, *Energy Environ. Sci.* **2024**, *17*, 885.

[34] Y. Liu, G. X. Tian, Y. J. Du, P. J. Shi, N. Li, Y. F. Li, Z. H. Qin, T. F. Jiao, X. M. He, H. Stretchable, *Adv. Funct. Mater.* **2024**, *34*, 2315813.

[35] W. T. Cao, H. Ouyang, W. Xin, S. Y. Chao, C. Ma, Z. Li, F. Chen, M. G. Ma, *Adv. Funct. Mater.* **2020**, *30*, 2004181.

[36] S. Dong, P. Wang, K. Abbas, *Comput. Sci. Rev.* **2021**, *40*, 100379.

[37] S. Sundaram, P. Kellnhofer, Y. Z. Li, J. Y. Zhu, A. Torralba, W. Matusik, *Nature* **2019**, *569*, 698.

[38] F. Wen, Z. X. Zhang, T. Y. He, C. K. Lee, *Nat. Commun.* **2021**, *12*, 5378.

[39] T. Kim, Y. Shin, K. Kang, K. Kim, G. Kim, Y. Byeon, H. Kim, Y. Gao, J. R. Lee, G. Son, T. Kim, Y. Jun, J. Kim, J. Lee, S. Um, Y. Kwon, B. G. Son, M. Cho, M. Sang, J. Shin, K. Kim, J. Suh, H. Choi, S. Hong, H. Cheng, H. G. Kang, D. Hwang, K. J. Yu, *Nat. Commun.* **2022**, *13*, 5815.

[40] Q. F. Shi, Z. X. Zhang, Y. Q. Yang, X. C. Shan, B. Salam, C. K. Lee, *ACS Nano* **2021**, *15*, 18312.

[41] D. S. Yu, K. Goh, H. Wang, L. Wei, W. C. Jiang, Q. Zhang, L. M. Dai, Y. Chen, *Nat. Nanotechnol.* **2014**, *9*, 555.

[42] N. N. Bai, L. Wang, Q. Wang, J. Deng, Y. Wang, P. Lu, J. Huang, G. Li, Y. Zhang, J. L. Yang, K. W. Xie, X. H. Zhao, C. F. Guo, *Nat. Commun.* **2020**, *11*, 07135.

[43] K. H. Lee, Y. Z. Zhang, Q. Jiang, H. Kim, A. A. Alkenawi, H. N. Alshareef, *ACS Nano* **2020**, *14*, 3199.

[44] Z. D. Sun, M. L. Zhu, X. C. Shan, C. K. Lee, *Nat. Commun.* **2022**, *13*, 5224.